

Discretization of the Generalized Porous Medium Equation with Discontinuous Coefficients Without Numerical Artifacts

Danielle C. Maddix^a, Margot Gerritsen^{a,b}, Luiz Sampaio^b, Anna Nissen^c

^a*Institute of Computational and Mathematical Engineering,
Stanford University*

^b*Energy Resources Engineering,
Stanford University*

^c*Dept. of Mathematics, University of Bergen, Norway*

Abstract

Numerical discretizations of the Generalized Porous Medium Equation (GPME) with discontinuous coefficients are analyzed with respect to the formation of numerical artifacts. In addition to the degeneracy and self-sharpening of the GPME with continuous coefficients, detailed in [1], increased numerical challenges occur in the discontinuous coefficients case. These numerical challenges manifest themselves in spurious temporal oscillations in second order finite volume discretizations with both arithmetic and harmonic averaging. The dynamic integral average, suggested in [2], leads to monotone temporal oscillations. In this paper, we propose a new dynamic average called the Shock-Based Averaging Method (SAM) that incorporates the shock position into the numerical scheme. The shock position is numerically calculated by discretizing the theoretical speed of the front from the GPME theory. This speed satisfies the jump condition for integral conservation laws. This newly developed method results in a non-oscillatory temporal profile, producing physically valid numerical results. We use SAM to demonstrate that the choice of averaging is not the cause of the oscillations, and that the shock position must be incorporated into the numerical scheme.

Keywords: Generalized Porous Medium Equation, Stefan problem, temporal oscillations, foam model, integral averaging, numerical shock detection, integral form, discontinuous coefficients, nonlinear degenerate parabolic equations, jump condition

1. Introduction

The purpose of the paper is to derive a robust numerical approach for the Generalized Porous Medium Equation (GPME) with discontinuous coefficients, given in Eqn. (1.1), as well as to identify the cause of the numerical artifacts reported in the literature for second order finite volume discretizations [1–3]. The GPME, commonly known as the Filtration Equation, can be expressed in both conservative and integral forms as given here for discontinuous coefficients:

$$\begin{aligned} p_t &= \nabla \cdot (k(p)\nabla p) \\ &= \Delta\Phi(p), \quad \text{where} \\ k(p) &= \begin{cases} k_{\max}, & p \geq p^* \\ k_{\min}, & p < p^*, \quad \text{and} \end{cases} \\ \Phi(p) &= \int_0^p k(\tilde{p})d\tilde{p}, \quad k(p) = \Phi'(p). \end{aligned} \tag{1.1}$$

Here, k_{\max} , k_{\min} and p^* are real positive constants.

Eqn. (1.1) is often used to illustrate the numerical challenges present in more complex porous media applications. For example, in van der Meer et al. [2] a foam model prototype is developed with $k_{\max} = 1$, $k_{\min} = \epsilon \rightarrow 0$ and $p^* = 0.5$. Following this paper, we will refer to $k(p)$ as the permeability and p as the pressure.

For $k_{\min} = 0$, $\Phi(p)$ in Eqn. (1.1) can be expressed as the positive part function

$$\Phi(p) = k_{\max}(p - p^*)_+ = \begin{cases} k_{\max}(p - p^*), & \text{if } p \geq p^*, \\ 0, & \text{otherwise.} \end{cases} \quad (1.2)$$

A similar expression can be found for another class of GPME, referred to as the Stefan problem, for which

$$\Phi(p) = \begin{cases} c_1(p - c_3)_+, & \text{if } p \geq 0, \\ c_2 p, & \text{otherwise,} \end{cases} \quad (1.3)$$

for arbitrary $c_1, c_2, c_3 \in \mathbb{R}$. Eqn. (1.2) can be interpreted as a special class of Stefan problem, where $c_1 = k_{\max}$, $c_3 = p^*$ and $p \geq 0$ always.

The Stefan Problem has been key to both the numerical and theoretical developments of the GPME. The Stefan Problem is used in modeling phase transitions, and was developed to study the evolution of a medium of two phases, namely water and ice [4]. Brattkus and Meiron [5] use the Stefan problem to model crystal growth. Sethian and Strain [6] and Chen et al. [7] develop a modified Stefan problem to model crystal growth as well as dendritic solidification.

Many other applications of the GPME can be found for continuous $k(p)$. The Porous Medium Equation (PME) subclass, where

$$k(p) = p^m, \quad m \geq 1, \quad (1.4)$$

is used to model gas flow through a porous medium [1, 4, 8]. Another application in thermodynamics is the superslow diffusion equation [1, 4], where

$$k(p) = \exp(-1/p). \quad (1.5)$$

Further applications of the GPME for continuous $k(p)$ are detailed in [1].

The continuous GPME already poses numerical challenges, caused by self-sharpening and degeneracy for near-zero $k(p)$ [1]. The discontinuous GPME in Eqn. (1.1) poses further numerical challenges. In [1], we propose alternate approaches to overcome these numerical difficulties based on Modified Equation Analysis. The same approach does not apply here because of the discontinuity in $k(p)$, which motivates this paper.

1.1. Understanding the Behavior of the GPME

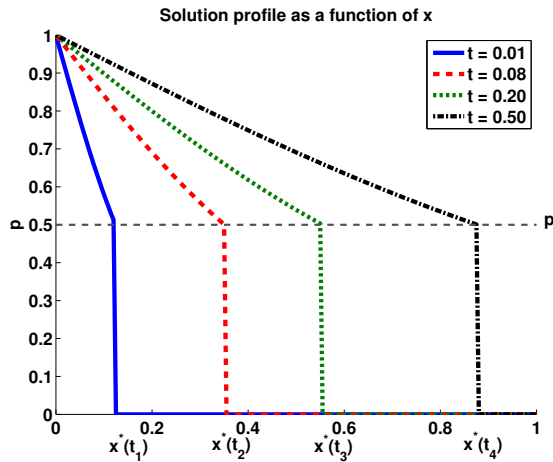


Figure 1: The exact solution of Eqn. (1.1), where $k_{\max} = 1$ and $k_{\min} = 0$, evolves as a rightward moving shock over time. The moving shock position is given by $x^*(t)$ and the fixed pressure value at the shock is given by $p^* = 0.5$.

The GPME in Eqn. (1.1) at first appears like a heat equation. Contrary to solutions of the heat equation, where the propagation speed is infinite, solutions of the GPME are known to have a finite speed of propagation [4]. This results from the degeneracy of the GPME for compactly supported initial data, and is a property that distinguishes the

GPME from classical parabolic theory. This degeneracy leads to self-sharpening and moving interface solutions, as illustrated in Figure 1. In addition, for certain compactly supported smooth initial data, the waiting time phenomenon can occur. This is discussed in the literature [9, 10] [11, Chapter 3] and is illustrated in Figure 3. Here, an interface is formed that moves, again at finite speed, only after the solution has sufficiently sharpened.

The theoretical propagation speed for compactly supported initial data is known and is given by Darcy's Law [4] as

$$V = - \lim_{x \rightarrow x^*(t)^-} \nabla v,$$

where

$$v = \int_0^p \frac{\Phi'(\tilde{p})}{\tilde{p}} d\tilde{p}, \quad (1.6)$$

and $x^*(t)$ is the shock position. Combining these expressions gives

$$V = - \lim_{x \rightarrow x^*(t)^-} \frac{\Phi'(p)\nabla p}{p} = - \lim_{x \rightarrow x^*(t)^-} \frac{k(p)\nabla p}{p}. \quad (1.7)$$

Eqn. (1.7) holds for any $k(p)$. For the PME in Eqn. (1.4), $k(p) = p^m$, and then

$$V_{\text{PME}} = - \lim_{x \rightarrow x^*(t)^-} \frac{\nabla p^m}{m}.$$

For the GPME in Eqn. (1.1), $k(p) = k_{\max} = 1.0$ to the left of the shock. Substituting the $k(p)$ limit into Eqn. (1.7) gives

$$V = - \lim_{x \rightarrow x^*(t)^-} \frac{\nabla p}{p} = - \lim_{x \rightarrow x^*(t)^-} \nabla \log(p). \quad (1.8)$$

The expression for the velocity V can also be expressed in terms of fluxes. The flux F for the integral conservation law in Eqn. (1.1) is given by

$$F(p) = -k(p)\nabla p = -\nabla\Phi(p). \quad (1.9)$$

Then, from Eqn. (1.7),

$$V = \frac{F(p_L)}{p_L}, \quad (1.10)$$

where $p_L \equiv \lim_{x \rightarrow x^*(t)^-} p(x, t)$. For a compactly supported initial condition and $k_{\min} = 0$, the flux and pressure values to the right of the shock are zero. In this case, the velocity in Eqn. (1.10) can be expressed in terms of the familiar jump condition for integral conservation laws as

$$V = \frac{F(p_L) - F(p_R)}{p_L - p_R}, \quad (1.11)$$

where $p_R \equiv \lim_{x \rightarrow x^*(t)^+} p(x, t)$ [4, 12].

1.2. Numerical Methods to Approach this Problem

The degeneracy, self-sharpening and nonlinearity of the GPME pose interesting numerical challenges. The numerical approaches used by practitioners vary based on the field. In the foam and porous media communities, central flux-based finite volume methods are widely employed to solve the related variable coefficients problem [13]

$$p_t = \nabla \cdot (k(x)\nabla p).$$

The coefficient $k(x)$ is defined at the cell-centers, and harmonic and arithmetic averaging are commonly used to compute the coefficient, which may be discontinuous, at the cell interface [1–3]. Harmonic averaging is often preferred in these problems because it leads to more physical solutions. This finite volume averaged-based approach has been extended to the nonlinear and more challenging GPME in Eqn. (1.1) for which the selection of the $k(p)$ averaging is not as straightforward. After carefully comparing arithmetic to harmonic averaging, Lipnikov et al. [3] prefer arithmetic averaging over harmonic for the PME with near-zero $k(p)$ in Eqn. (1.4). An integral average is proposed

in van der Meer et al. [2] for the discontinuous GPME in Eqn. (1.1). We will address these results further in Section 5. With these average-based approaches, it is difficult to satisfy the jump condition in Eqn. (1.11). Violation of this condition manifests itself in locking and spurious temporal oscillations, as illustrated in Figures 2 and 3.

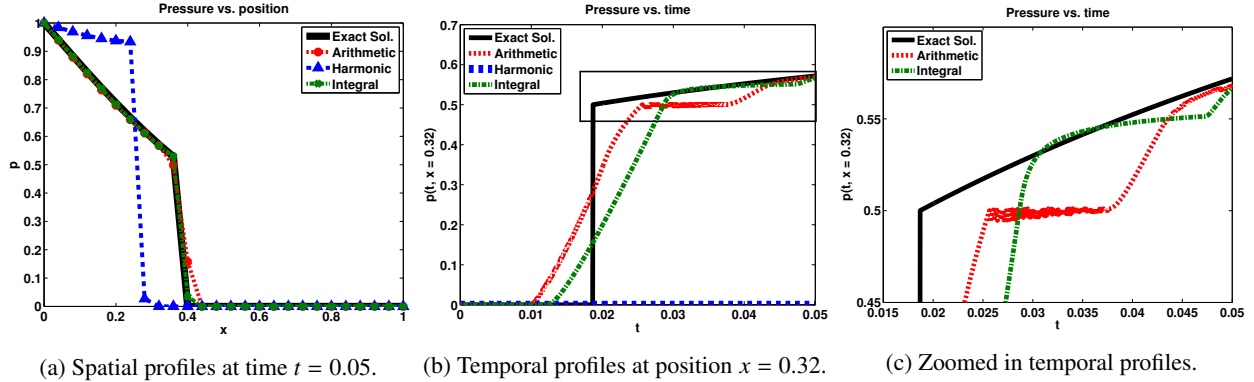


Figure 2: Comparison of various averages, where $k_{\max} = 1$, $k_{\min} = 0$ and $p^* = 0.5$. The spatial step size $\Delta x = 0.04$ and the time step size $\Delta t = \Delta x^2/32$.

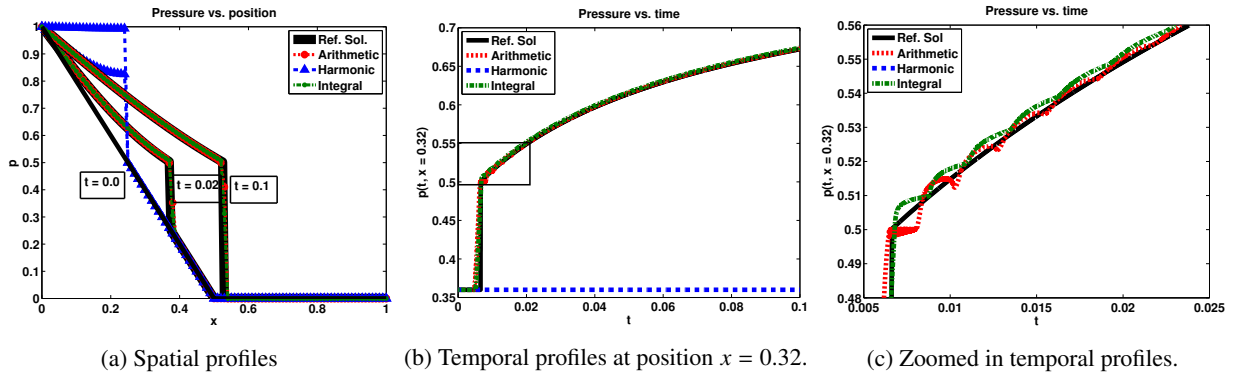


Figure 3: Comparison of various averages, where $k_{\max} = 1$, $k_{\min} = 0$ and $p^* = 0.5$ for a waiting time phenomenon example. The piecewise linear initial condition self-sharpens until it is sharp enough for the support interface position to move rightward at later times past the initial interface position at $x = 0.5$. The spatial step size $\Delta x = 0.01$ and the time step size $\Delta t = \Delta x^2/32$.

Adaptive and moving mesh approaches have been applied to this problem also with increased refinement near the shock. In [8], for example, a finite element moving mesh method for the PME with $k(p)$ in Eqn. (1.4) is developed. Adaptive Mesh Refinement (AMR) will be discussed further in Section 5.

In the crystal application communities, numerical work has been done on solving the Stefan problem, as detailed in [14–17] and the references therein. In [18, 19], an enthalpy scheme for Stefan problems is introduced. This method consists of a compact finite difference stencil with an implicit temporal scheme. The shock position is not incorporated into the scheme, and the error is observed to be concentrated at the moving interface. Brattkus and Meiron [5] show that finite difference and finite element methods that do not take special care at the interface result in a significant error of $O(\sqrt{\Delta x})$. They propose a method based on an integral equation formulation that requires an additional integral evaluation.

In two-phase flow applications of the Stefan problem, level set methods [20] could also be useful in tracking the evolving interface. Thus far, they have not been applied to Eqn. (1.1), but in Sethian and Strain [6] and Chen et al. [7], level set methods are used for a related problem with Stefan boundary conditions. A modified Stefan problem is also solved in Zhao et al. [21] using a phase-field method. Phase-field methods converge as the interface thickness parameter tends to zero.

1.3. Main Goals of this Paper

The first goal of this paper is to devise an accurate numerical method for Eqn. (1.1) that does not exhibit the numerical errors observed in the literature. The newly developed Shock-Based Averaging Method (SAM) is discussed in Section 2. Incorporation of the shock position is key. Section 3 discusses the derivation of SAM when the shock position is known. The shock position can also be approximated using the jump condition, which is detailed in Section 4.

The second goal is to shed light on the origin of the numerical problems reported in the literature for finite volume averaged-based approaches. In Section 5, we cast SAM in this same framework to help identify what is lacking in these approaches. The main problem is that these discretizations contain none or insufficient information about the shock and therefore the whole approach must be modified to avoid the numerical artifacts.

2. Proposed Numerical Method: Shock-Based Averaging Method (SAM)

Due to the discontinuities in $k(p)$ and p , we adopt a finite volume approach to the integral form of the governing equation (1.1). We first define a finite volume grid with cell-centers x_j for $j = 1, \dots, N + 1$. The boundaries of the domain are at x_1 and x_{N+1} , respectively and the corresponding pressures are fixed by Dirichlet boundary conditions. The remaining $N - 1$ degrees of freedom p_j , and the corresponding coefficients k_j , are defined at the nodes x_j for $j = 2, \dots, N$. We define control volumes CV_j with width Δx_j . The cell faces $x_{j+1/2}$ of each CV_j are at a distance of $\Delta x_j/2$ from the cell-centers x_j . We assume that the solution is monotone and non-increasing, and that the shock is located between x_i and x_{i+1} , such that $p_i \geq p^* \geq p_{i+1}$.

The semi-discrete numerical discretization for CV_j with volume Δx_j is given by

$$\Delta x_j \frac{dp_j}{dt} = F_j^- - F_j^+, \quad (2.1)$$

where F_j^- represents the in-flux and F_j^+ represents the out-flux of CV_j . The numerical fluxes

$$F_j^+ = -k_{j+1/2} \frac{p_{j+1} - p_j}{\Delta x}, \quad j \neq i, \quad (2.2)$$

and

$$F_j^- = -k_{j-1/2} \frac{p_j - p_{j-1}}{\Delta x}, \quad j \neq i + 1, \quad (2.3)$$

are defined at all faces away from the shock cell with the standard two-point flux approximation, where $\Delta x \equiv \Delta x_j$. The coefficient $k_{j+1/2}$ at the cell face represents a local average of its neighboring coefficients. Then, for any two-neighbor average away from the shock cell, the coefficient is constant and given by

$$k_{j+1/2} = \begin{cases} k_{\max}, & 1 \leq j \leq i - 1, \\ k_{\min}, & i + 1 \leq j \leq N. \end{cases} \quad (2.4)$$

Analogous definitions are used for $j - 1/2$. Because of the discontinuity, Eqns. (2.2)-(2.3) cannot be used for the flux at the cell interface $x_{i+1/2}$.

2.1. Formulation of the Fluxes near the Shock

To estimate the fluxes out of CV_i and into CV_{i+1} , we borrow ideas from hyperbolic systems [22] and place a control volume around the discontinuity. Figure 4 shows the auxiliary finite volume grid with the additional control volume CV_* around the physical shock position $x^*(t)$, where $p(x^*(t), t) \equiv p^*$ is defined. Figure 4 also shows $\Delta x^*(t)$ as the distance between x_i and $x^*(t)$, where $0 \leq \Delta x^*(t) \leq \Delta x$. We then remove the cell face at position $x_i + \Delta x/2$ and add the cell faces of CV_* . The new cell faces are chosen to be centrally located at a distance of

$$\frac{|x^*(t) - x_i|}{2} \equiv \frac{\Delta x^*}{2},$$

from x_i and $x^*(t)$, and a distance of

$$\frac{|x^*(t) - x_{i+1}|}{2} \equiv \frac{\Delta x - \Delta x^*}{2},$$

from $x^*(t)$ and x_{i+1} . We have effectively added an additional degree of freedom p^* at $x^*(t)$. Here p^* is known, and it does not actually need to be computed, but we present the approach in its general form for future extensions.

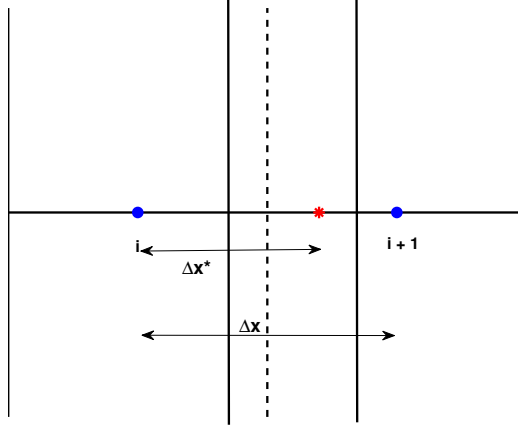


Figure 4: Illustration of the additional control volume CV_* around the shock position $x^*(t)$. The grid points x_i and x_{i+1} are depicted by the blue dots, and $x^*(t)$ is depicted by the red star. The dashed line represents the deleted cell face between CV_i and CV_{i+1} . The new cell faces are located at a distance $\Delta x^*(t)/2$ from x_i and $[\Delta x - \Delta x^*(t)]/2$ from x_{i+1} .

With the additional control volume, we can now define the necessary out-flux F_i^+ of CV_i and in-flux F_{i+1}^- of CV_{i+1} . The coefficient at each of the new cell faces is known. By the monotonicity of p , for any $p(x, t)$ to the left of the interface, $k(p(x, t)) = k_{\max}$. Similarly, for any $p(x, t)$ to the right of the interface, $k(p(x, t)) = k_{\min}$. Based on the known coefficient values at the faces and the face-centered grid, the second-order fluxes are given by

$$F_i^+ = -k_{\max} \frac{p^* - p_i}{\Delta x^*}, \quad (2.5)$$

at the cell face between x_i and x^* and

$$F_{i+1}^- = -k_{\min} \frac{p_{i+1} - p^*}{\Delta x - \Delta x^*}, \quad (2.6)$$

at the cell face between x^* and x_{i+1} . The resulting scheme is conservative because F_i^+ is equal to the in-flux F_{i+1}^- of CV_* , by definition and similarly F_{i+1}^- is equal to the out-flux F_i^+ of CV_* . The fluxes are then substituted into the semi-discrete equation (2.1), where the cell volumes are now given by $\Delta x_i = (\Delta x + \Delta x^*)/2$ and $\Delta x_{i+1} = \Delta x - \Delta x^*/2$, respectively.

For $k_{\min} = 0$, we can relate the expression for F_i^+ in Eqn. (2.5) to the expression for $\Phi(p) = k_{\max}(p - p^*)_+$ in Eqn. (1.2) for the Stefan problem. The analytical flux $F(p_L)$ is given by $-\nabla\Phi(p_L)$ in Eqn. (1.9). The numerical flux F_i^+ can be interpreted as approximating this gradient with an upwind discretization as

$$-\frac{\Phi(p^*) - \Phi(p_i)}{\Delta x^*} = -k_{\max} \frac{p^* - p_i}{\Delta x^*} = F_i^+.$$

We see that the numerical flux jump is a first-order approximation of the jump condition in Eqn. (1.11).

Round-off errors can arise when the shock location approaches the grid points x_i and x_{i+1} . At these times, the denominators in Eqn. (2.5) and Eqn. (2.6) approach zero. To avoid problems, we specify a tolerance of ϵ that is proportional to Δx . If $\Delta x^* \leq \epsilon$, we neglect the leftmost portion near x_i , and set $k_{i+1/2} = k_{\min}$ for CV_i . Similarly, if $\Delta x - \Delta x^* \leq \epsilon$, we ignore the rightmost portion near x_{i+1} , and set $k_{i+1/2} = k_{\max}$ for CV_{i+1} . We then use these coefficients in the standard two-point flux approximation in Eqns. (2.2) and (2.3).

We will refer to the above approach as the Shock Based-Averaging Method (SAM).

3. SAM Numerical Results: Exact Shock Location

In the numerical results presented throughout the paper, the test problem is given by Eqn. (1.1) with $k_{\max} = 1.0$, $k_{\min} = 0.0$ and $p^* = 0.5$. The choice of k_{\max} and p^* is arbitrary, while k_{\min} is set to zero to test the behavior of the numerical method in the degenerate case. The algorithm also works for arbitrarily small k_{\min} . The fixed Dirichlet boundary conditions are given by

$$\begin{aligned} p(0, t) &= 1.0, \quad \forall t \geq 0, \\ p(1, t) &= 0.0, \quad \forall t \geq 0. \end{aligned} \tag{3.1}$$

The initial condition is displayed in Figure 5.

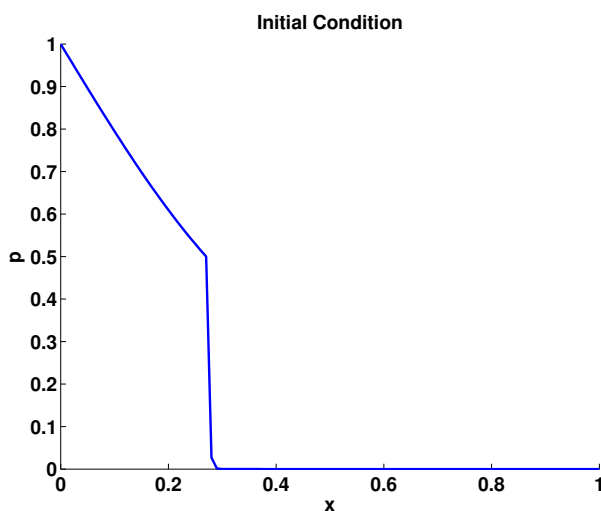


Figure 5: Spatial profile at time $t = 0$.

For the representative test problem, an analytical solution exists, and is used to verify the implementation through detailed convergence studies. The derivation of the exact solution is generalized for arbitrary k_{\max} in Appendix A. In this section, we use the exact shock position to compute $\Delta x^*(t) \equiv |x^*(t) - x_i|$, where

$$x^*(t) = \alpha \sqrt{t}, \quad \alpha = 2 \sqrt{k_{\max} z_1},$$

and z_1 is the solution to the nonlinear equation in Eqn. (A.4). In the following section, we will show how the shock location can be approximated, if it is not available.

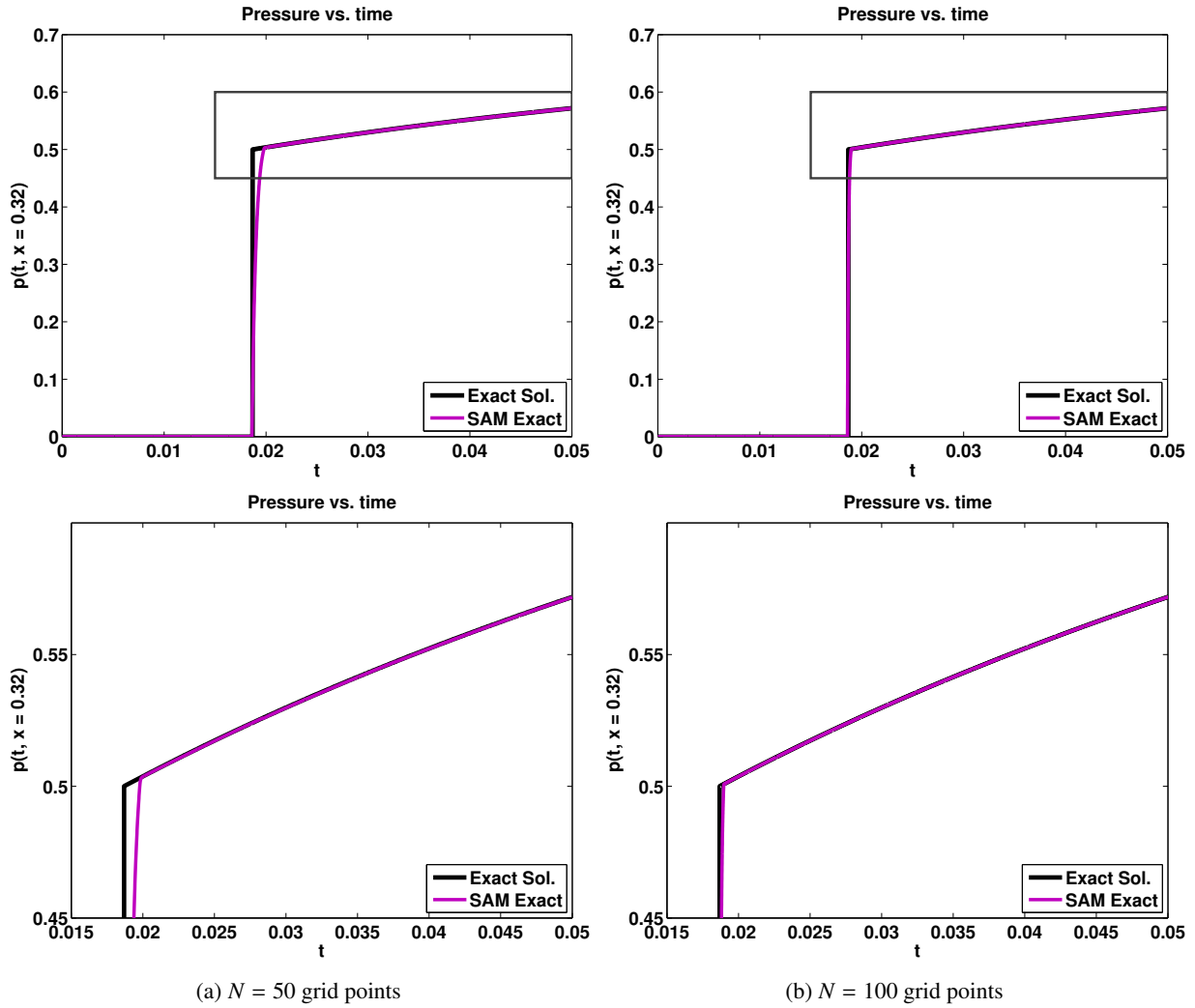


Figure 6: Temporal profiles at position $x = 0.32$ with $\Delta t = \Delta x^2/32$.

In Figure 6, the numerical solution is plotted at the arbitrary position $x = 0.32$ over time. By self-similarity of the solution [1, 4, 8], the temporal plots have the same profile for any x -coordinate that the front has passed through. Figure 6 illustrates that the numerical solution with SAM has an accurate and non-oscillatory temporal profile, even on a coarse grid.

Figure 7 reveals that the shock location is accurate in space for this moving front problem. The self-sharpening nature of the GPME [1, 4, 8] is depicted, by the smooth lower corner in the initial condition in Figure 5 evolving into a sharp corner in Figure 7. Figure 7 also illustrates the sharp capture of the shock.

The results in this section show that the numerical artifacts discussed in Section 1.2 are not present with SAM.

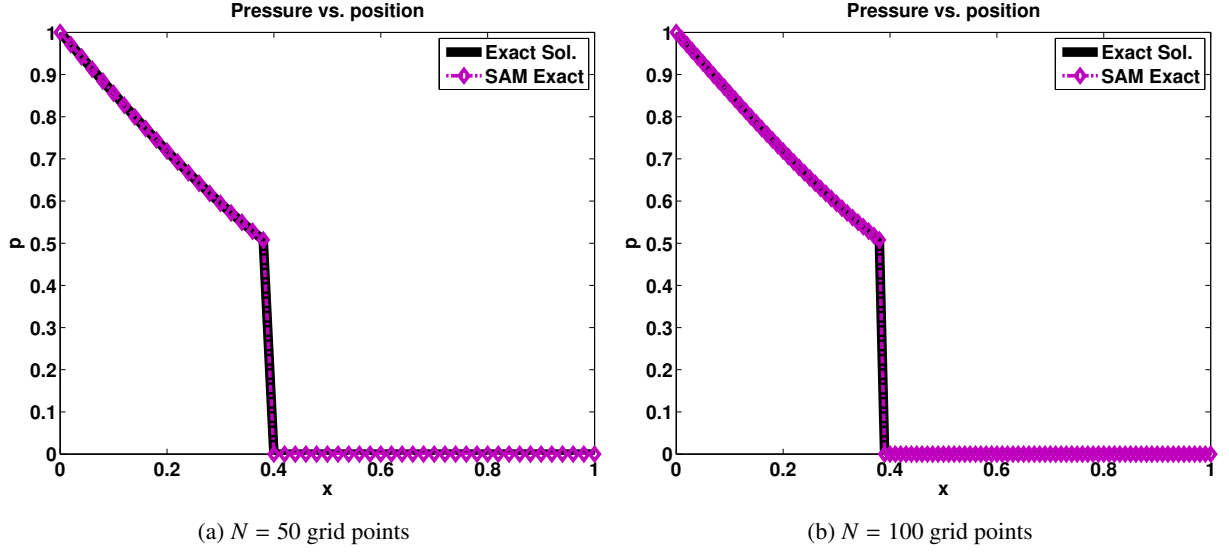


Figure 7: Spatial profiles at time $t = 0.05$ with $\Delta t = \Delta x^2/32$.

4. SAM Numerical Results: Approximate Shock Location

The method in the prior section can be extended to more general GPME problems, where the exact shock position is not known. The finite speed of propagation property and theoretical speed of the front for the GPME, discussed in Section 1.1, can be utilized to numerically approximate the shock location. Again the fluxes in Eqns. (2.5) and (2.6) are used with the difference that $\Delta x^*(t)$ is numerically calculated. In this section, we show that this approximation does not introduce numerical artifacts, such as temporal oscillations.

We discretize V in Eqn. (1.8) with upwinding for the derivative as

$$\hat{V} = -\frac{p_i - p_{i-1}}{\Delta x p_i}, \quad (4.1)$$

where i is the index, such that $p_i \geq p^* \geq p_{i+1}$. Eqn. (4.1) can be interpreted as an approximation of the jump condition in Eqn. (1.10), where p_L is approximated by p_i and $p_R = 0$. For problems where p_R is not initially zero, such as the waiting time problem in Section 1.2, we can also use a discrete approximation to Eqn. (1.11). Care must be taken numerically when approximating p_R in Eqn. (1.11), since p_{i+1} is not guaranteed to be zero: all that is guaranteed is that $0 \leq p_{i+1} \leq p^*$. In this case, we use p_{i+2} to approximate p_R .

To obtain the numerical shock position, a simple time integration is implemented. We let ξ^n represent the approximate $x^*(t)$ at time step $n \geq 0$ and substitute

$$\Delta x^*(t) \approx \xi^n - x_i, \quad (4.2)$$

into the expressions for the fluxes in Eqns. (2.5) and (2.6). We integrate the approximate shock speed in Eqn. (4.1) in time, using the following update

$$\xi^{n+1} = \xi^n + \Delta t \hat{V}. \quad (4.3)$$

We assume that the initial position ξ^0 is known from the problem definition or can also be approximated.

We can also approximate $\Delta x^*(t)$ using a level set method [20]. In the level set method, the interface $x^*(t)$ is represented by the zero level set $\{x \mid \phi(x, t) = 0\}$ of a signed distance function $\phi(x, t)$. Using the velocity V of the interface in Eqn. (1.8), the evolution equation can be written in terms of $\phi(x, t)$ as

$$\phi_t + V \cdot \nabla \phi = 0. \quad (4.4)$$

The level set equation (4.4) can be solved numerically using Forward Euler in time and upwinding for the gradient, where V is discretized as \hat{V} in Eqn. (4.1). Since $\Delta x^*(t)$ is defined as the distance from the shock or interface $x^*(t)$ to

the grid point x_i , $\Delta x^*(t)$ can be calculated by $|\phi(x_i)|$. Solving Eqn. (4.4) for ϕ_i^n and setting $\Delta x^*(t) \approx |\phi_i^n|$ gives the same results as solving Eqns. (4.2)-(4.3).

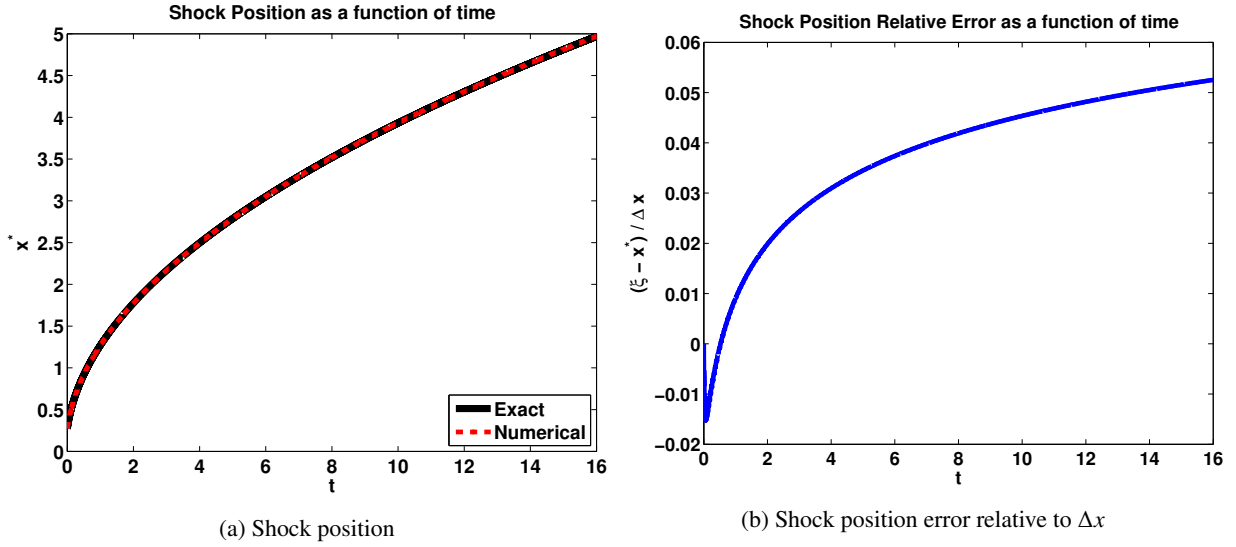


Figure 8: Comparison of the temporal profiles of the shock position and relative error for $\Delta x = 0.04$ and $\Delta t = \Delta x^2/32$.

Figures 8a and 8b illustrate the long-time behavior of the numerical shock position evolution. Figure 8a displays that the numerical shock position aligns with the exact shock position as a function of time. We see that the shock position evolution is accurately captured without oscillations. Figure 8b shows that the maximum error in the shock position relative to Δx does not exceed 6%. Both plots verify the numerical implementation, and show that there is no significant accuracy loss in estimating the shock position using Eqn. (4.3).

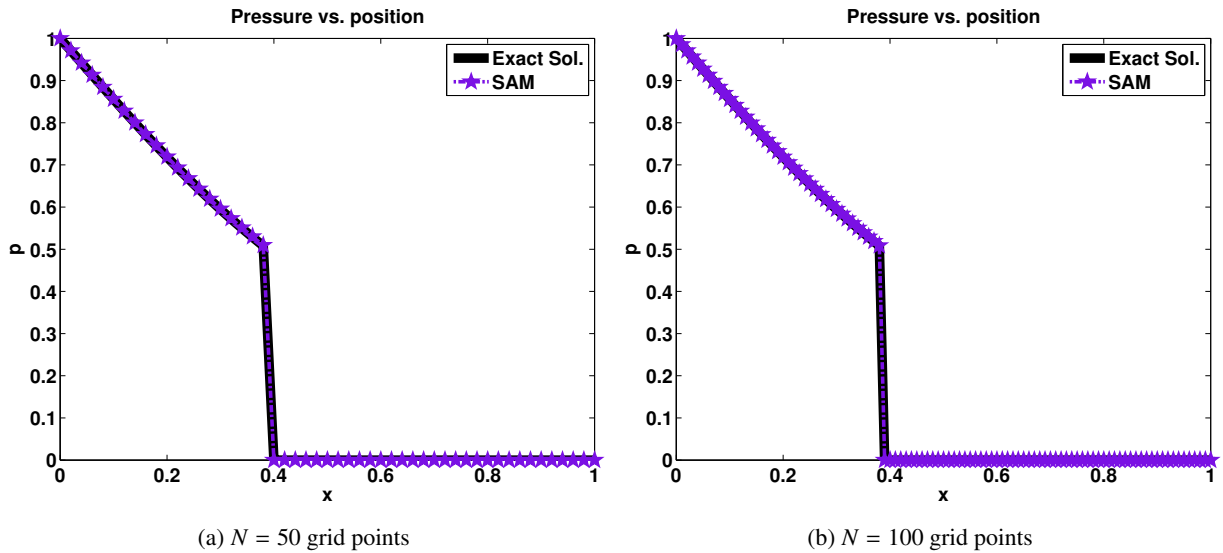


Figure 9: Spatial profiles at time $t = 0.05$ with $\Delta t = \Delta x^2/32$.

The results in Figures 9 and 10 on the same test case from the prior section show that there is no significant change in the behavior of the SAM solution with the approximate shock speed than with exact shock speed in the

prior section. Figure 9 shows that the shock position capture is still accurate, and Figure 10 shows that there are no spurious temporal oscillations nor any other numerical artifacts.

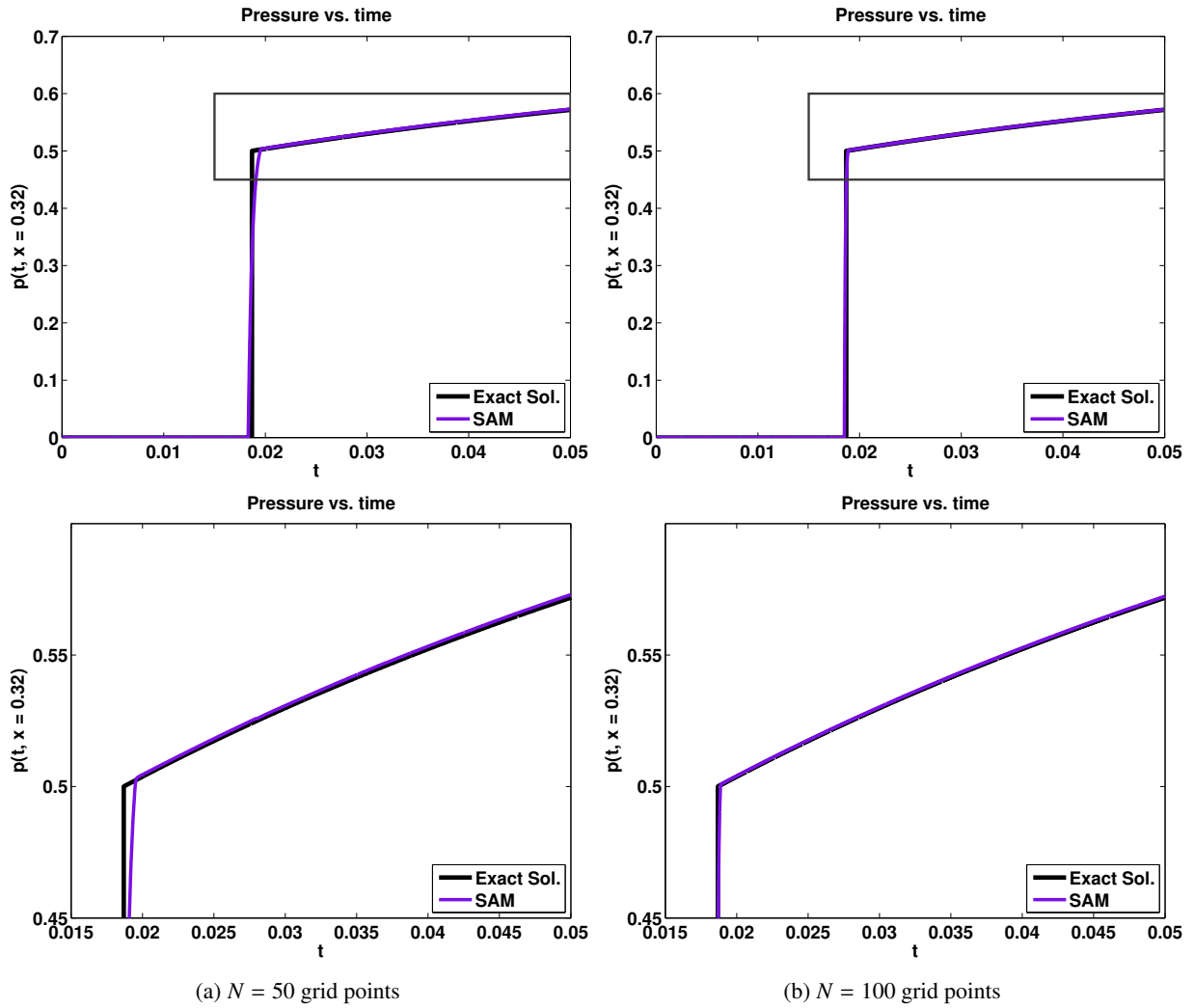


Figure 10: Temporal profiles at position $x = 0.32$. with $\Delta t = \Delta x^2/32$.

Figures 11a-11c show results for SAM for the waiting phenomenon problem discussed in Section 1.1. This is an interesting problem because for this initial condition, the exact solution is not known. The figures show that the SAM solution is accurate and does not possess the numerical artifacts shown in Figure 3.

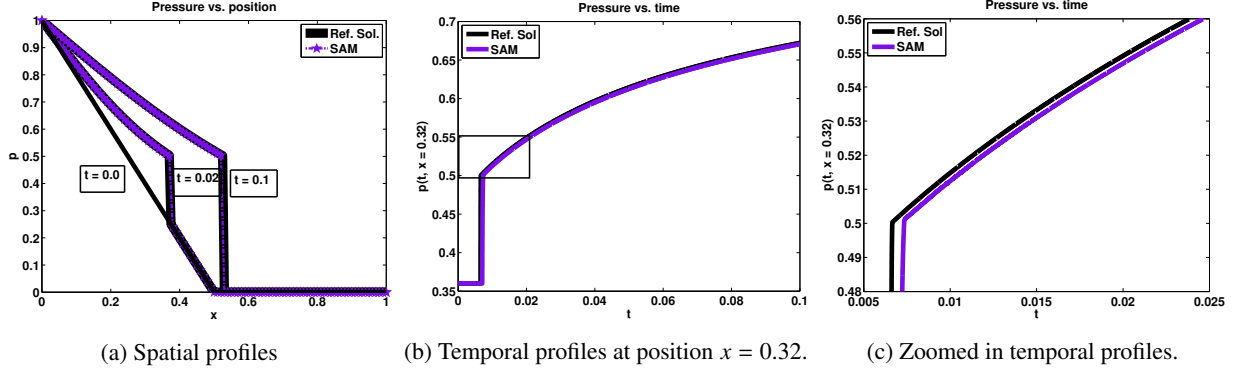


Figure 11: SAM numerical solution with $N = 100$ grid points and $\Delta t = \Delta x^2/32$ for the waiting time phenomenon example from Figure 3.

5. Average-based approaches

In Section 2, we formulated SAM as a shock tracking method. In this section, we show results for commonly used averaging methods from the literature, discussed in Section 1.2. We also show how SAM can be expressed in this averaging framework to explain the cause of the temporal oscillations seen in the literature.

We implement the finite volume average-based methods using the Forward in Time, Central in Space (FTCS) discretization on a uniform Cartesian grid, as is commonly done in this literature [2, 3]. The numerical fluxes are given by

$$F_j^+ = -k_{j+1/2} \frac{p_{j+1} - p_j}{\Delta x}, \quad (5.1)$$

and

$$F_j^- = -k_{j-1/2} \frac{p_j - p_{j-1}}{\Delta x}, \quad (5.2)$$

for an arbitrary average $k_{j+1/2}$ of the neighboring coefficients at the cell face $x_{j+1/2}$ for all $j = 1, \dots, N$. For validation, we successfully repeated the test case presented for the arithmetic and integral average in van der Meer et al. [2].

In this section, we use the test case corresponding to the initial condition in Figure 5.

5.1. Arithmetic and Harmonic Averages

In the FTCS finite volume scheme with arithmetic

$$k_{j+1/2}^A = \frac{k_j + k_{j+1}}{2}, \quad (5.3)$$

and harmonic

$$k_{j+1/2}^H = \frac{2k_j k_{j+1}}{k_j + k_{j+1}}, \quad (5.4)$$

averaging, no special care is taken to compute the pressure gradient across the interface. The fluxes in and out of the control volumes surrounding the shock are discretized using Eqns. (5.1)-(5.2). The corresponding arithmetic fluxes are given by

$$F_i^{+A} = F_{i+1}^{-A} = -k_{i+1/2}^A \frac{p_{i+1} - p_i}{\Delta x}. \quad (5.5)$$

The analogous expression holds for the harmonic fluxes F_i^{+H} and F_{i+1}^{-H} , where the arithmetic average $k_{i+1/2}^A$ in Eqn. (5.5) is replaced with the harmonic average $k_{i+1/2}^H$. The temporal and spatial results are discussed below.

The temporal plots at $x = 0.32$ in Figure 12 reveal that the numerical interface with harmonic averaging is locked, and does not advance to this position. Figure 13 shows the spatial evolution and we again see the locking with harmonic averaging. The numerical solution with harmonic averaging in Figure 13 evolves to a step function with values at 1 and 0. Eqn. (5.4) explains the locking numerical artifact, since $k_{j+1/2}^H = 0$ when either coefficient is

zero. This locking property of the harmonic average is also known as blocking. Blocking can be desirable in variable coefficient problems, where the interface separates a permeable and impermeable material [13].

We can relax $k_{\min} = 0$ to $k_{\min} = \epsilon$ for some small $\epsilon > 0$. For $\epsilon = 0.01$, the numerical solution with harmonic averaging no longer locks, but is lagging behind the true front location. From Eqn. (5.4), we see that $k_{i+1/2}^H$ favors the smaller coefficient and is approximately equal to 2ϵ , as the shock moves through the interval $[x_i, x_{i+1}]$. The constant and small permeability at the cell face results in a solution whose numerical speed is too slow. Grid dependent oscillations are present in its temporal profile.

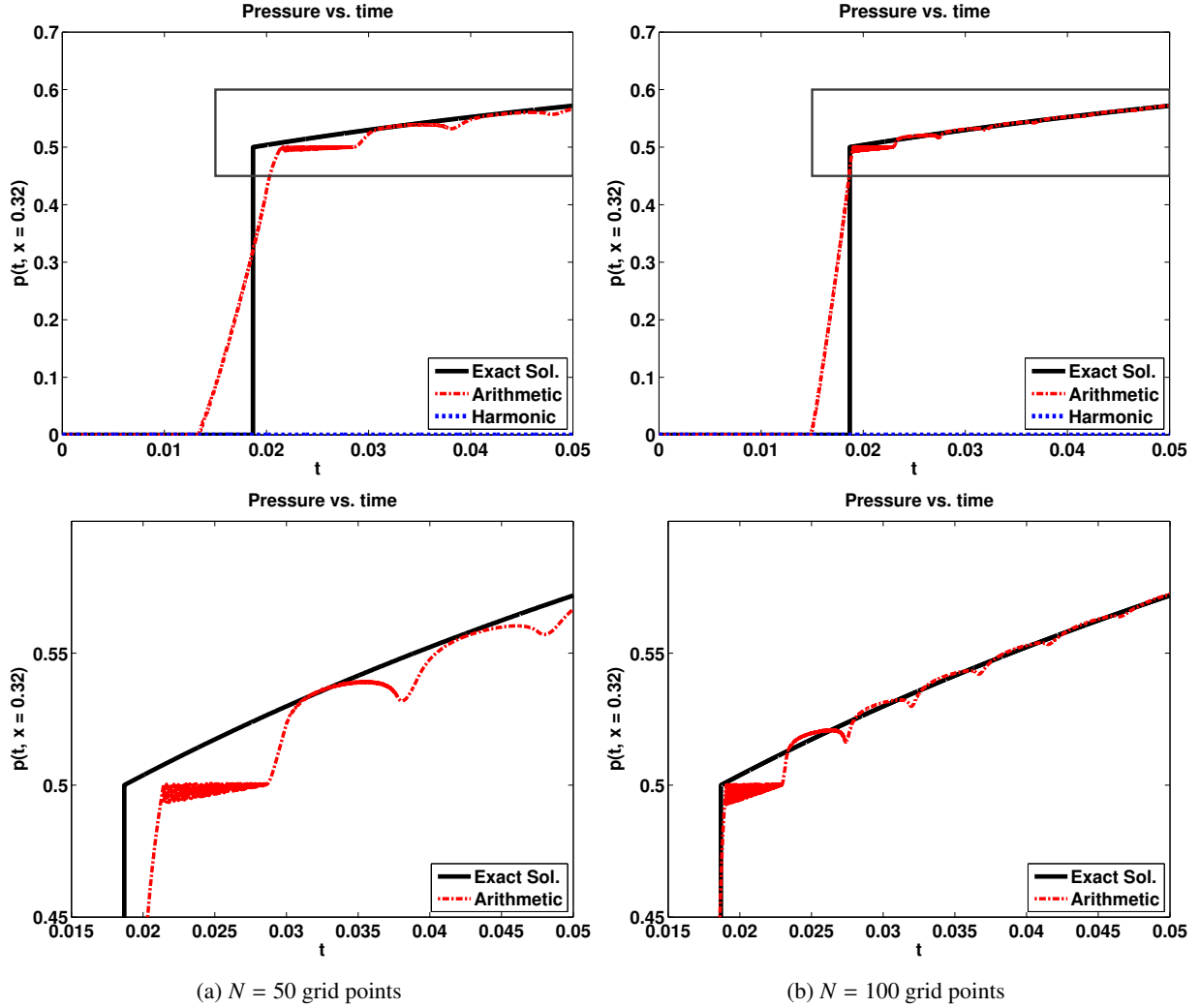


Figure 12: Temporal profiles at position $x = 0.32$ with $\Delta t = \Delta x^2/32$.

The numerical solutions depicted in Figures 12 and 13 also show that the arithmetic average is not attractive. In Figures 12 and 13, we see that the numerical solution with arithmetic averaging does not sharply capture the shock. Figure 12 shows spurious oscillations of low and high frequency in solutions with the arithmetic average. The low frequency oscillations are grid dependent. The high frequency oscillations are apparent in the zoomed in region around the pressure shock value of $p^* = 0.5$.

It is interesting to note that Figure 13 shows no spatial oscillations in the solution with arithmetic averaging, while there are temporal oscillations in Figure 12. The numerical solutions satisfy the total variation diminishing (TVD) property [23] that was designed to eliminate spurious spatial oscillations from dispersion in hyperbolic conservation

laws. The total variation $TV(p^n) = \sum_i |p_{i+1}^n - p_i^n| = 1$ for all n for both the arithmetic and harmonic solutions, matching that of the true solution. To determine the presence of the temporal oscillations, another metric must therefore be used.

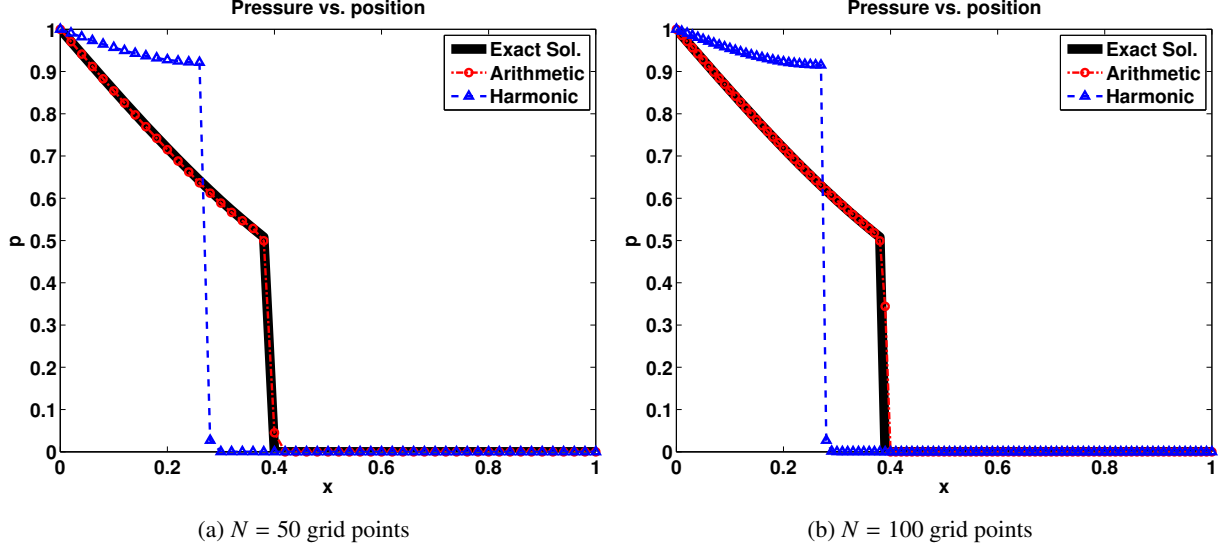


Figure 13: Spatial profiles at time $t = 0.05$ with $\Delta t = \Delta x^2/32$.

In Maddix et al. [1], we looked at numerical artifacts associated with arithmetic and harmonic averaging for the GPME with continuous coefficients for $k(p)$ in Eqns. (1.4)-(1.5). For these problems, temporal oscillations were only observed in solutions with harmonic averaging. Modified Equation Analysis was utilized to identify an anti-diffusive term contributing to the temporal oscillations in solutions with harmonic averaging. The Modified Harmonic Method (MHM) was developed to counteract the anti-diffusive term and remove the temporal oscillations. The MHM approach is not applicable to the foam model prototype discussed in this paper, since $k(p)$ in Eqn. (1.1) is not differentiable with respect to p . The main difference in the results here is the presence of the temporal oscillations in numerical solutions with arithmetic averaging. The lower frequency grid dependent oscillations were analyzed in [1] for discretizations with harmonic averaging. The high frequency oscillations are an additional numerical artifact with arithmetic averaging that were not observed for the harmonic average in [1].

The low frequency temporal oscillations have been studied in the literature [1, 2, 24, 25]. It has been shown in these works that the temporal oscillations occur as the front crosses a grid cell. The spurious oscillations then do not vanish with grid refinement. The frequency increases and the amplitude decreases, as the number of grid points increases. The differences in frequency and amplitude are illustrated by the solutions for $N = 50$ in Figure 12a and $N = 100$ in Figure 12b. Another observed characteristic of these oscillations is that the amplitude decreases as shock moves further away from the pressure probe point.

We now look at the behavior of the high frequency oscillations that were also observed in [2]. Figures 14a-14b illustrate the temporal profile on a shorter time interval, where the high frequency oscillations occur for pressure values near $p^* = 0.5$. We see that the pressure p_{i+1} is slowly increasing, until it crosses the threshold at $p^* = 0.5$. The corresponding permeability k_{i+1} then jumps from $k_{\min} = 0$ to $k_{\max} = 1$, according to the model for $k(p)$ in Eqn. (1.1). The arithmetic average $k_{i+3/2}^A$ in Eqn. (5.3) jumps from 0 to 0.5, as illustrated in Figures 14a-14b. The increase in $k_{i+3/2}^A$ causes the pressure to drop below $p^* = 0.5$ and $k_{i+3/2}^A$ to jump back down to 0 at the next time step. The cycle then repeats itself.

We use the FTCS discretization to explain the effect of the jump in $k_{i+3/2}^A$ on the pressure value at the next time step. We discretize the semi-discrete equation (2.1) with Forward Euler in time and substitute in the arithmetic fluxes to obtain

$$p_{i+1}^{n+1} = p_{i+1}^n + \frac{\Delta t}{\Delta x} \left(-k_{i+1/2}^A \left[\frac{p_{i+1}^n - p_i^n}{\Delta x} \right] + k_{i+3/2}^A \left[\frac{p_{i+2}^n - p_{i+1}^n}{\Delta x} \right] \right), \quad (5.6)$$

where n is a time step before the pressure drop and $p_{i+1}^n \geq 0.5$. The first term in Eqn. (5.6) is small in magnitude, since $p_i^n \approx 0.5$. The second term has a larger pressure gradient, since $p_{i+2}^n \approx 0$. The second term in Eqn. (5.6) is also negative and so the increase in $k_{i+3/2}^A$ results in the drop in p_{i+1}^{n+1} . The permeability $k_{i+3/2}^A = 0$ at the following time steps, until the pressure crosses the threshold again.

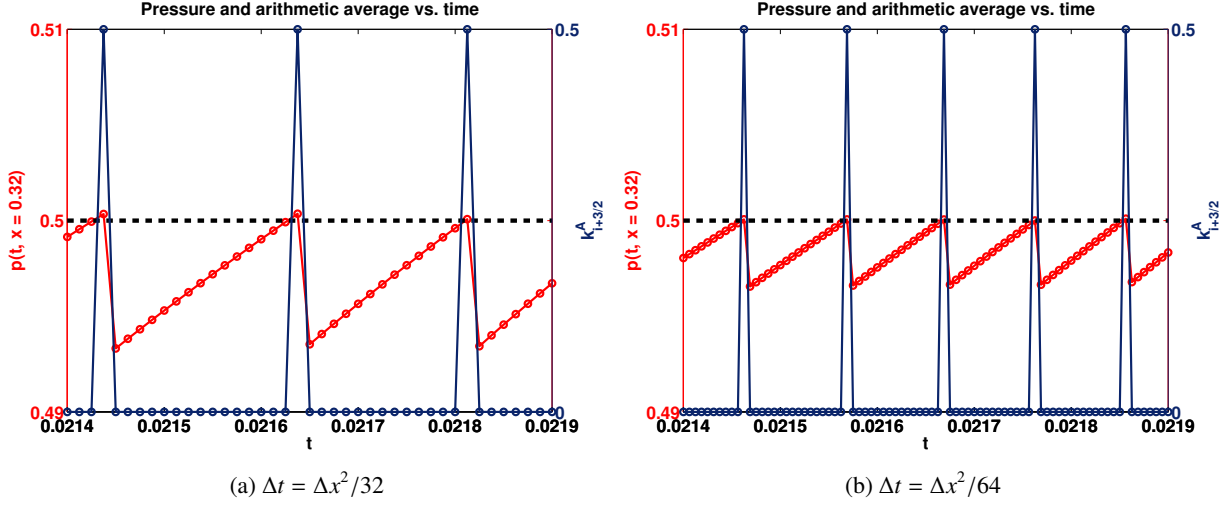


Figure 14: Zoomed in region of the high frequency temporal oscillations near $p^* = 0.5$ in the left cell p_{i+1} for the arithmetic average $k_{i+3/2}^A$ with $N = 50$ grid points.

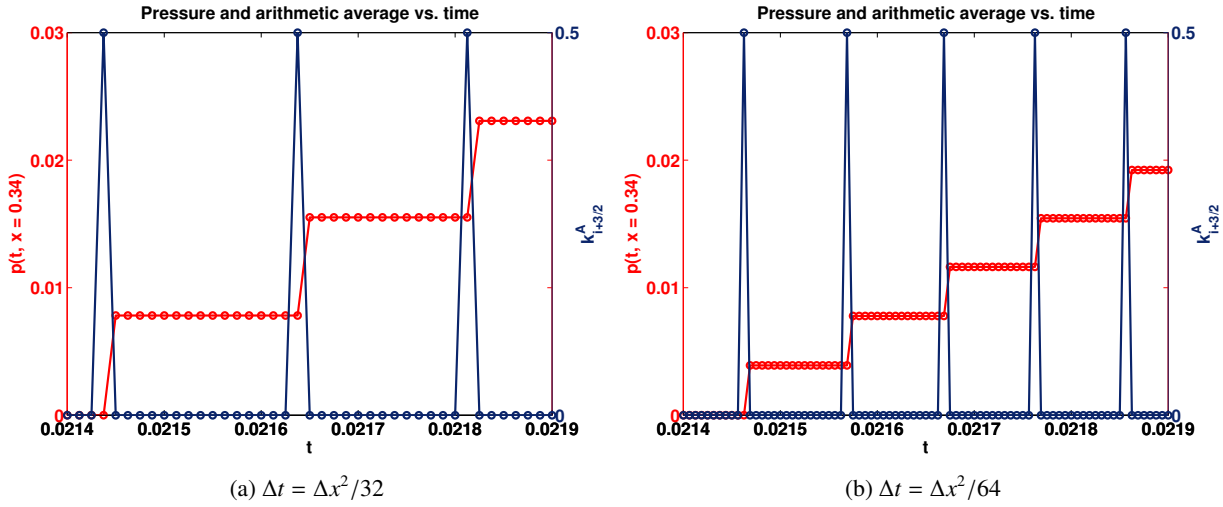


Figure 15: Zoomed in region of the pressure in the right cell p_{i+2} for the arithmetic average $k_{i+3/2}^A$ with $N = 50$ grid points.

As p_{i+1} is increasing and is below the threshold, $k_{i+1/2}^A$ is fixed at 0.5, regardless of the shock position in the cell. From Eqn. (5.6), we see that the positive quantity $\Delta t / (2\Delta x^2) [p_i^n - p_{i+1}^n]$ is added to the current pressure value at each time step. The constant arithmetic average at the interface $x_{i+1/2}$ allows the pressure to artificially increase above $p^* = 0.5$, resulting in the high frequency oscillations. The arithmetic average is known to cause leakage, by allowing flow to diffuse across the interface too quickly [13].

Figures 14a-14b also show that the high frequency oscillations are dependent on the time step size. As Δt is decreased by half, the number of oscillations in Figure 14b doubles from those in Figure 14a. The amplitude of the

high frequency oscillations also decreases, as Δt decreases. The amplitude decrease is expected from Eqn. (5.6), since the additional term is proportional to Δt . In [2], it is observed that as the time step is decreased, the arithmetic average solution in the high frequency region reaches a constant state at $p^* = 0.5$, rather than converging to the true solution.

Figures 14a-14b display the profile of p_{i+1} over a time window when the shock is in the interval $[x_i, x_{i+1}]$. In Figures 15a-15b, we now look at the profile of p_{i+2} over the same time window to see the effect of the jump in $k_{i+3/2}^A$ on the neighboring cell. Figures 15a-15b show that the profile of p_{i+2} is an increasing piecewise constant. Since p_{i+2} and p_{i+3} are both less than p^* , $k_{i+5/2}^A = 0$ and the pressure update for p_{i+2}^{n+1} reduces to

$$p_{i+2}^{n+1} = p_{i+2}^n + k_{i+3/2}^A (p_{i+1}^n - p_{i+2}^n) \frac{\Delta t}{\Delta x^2}. \quad (5.7)$$

Eqn. (5.7) shows that at the times when $p_{i+1}^n < p^* = 0.5$, $k_{i+3/2}^A = 0$, and so $p_{i+2}^{n+1} = p_{i+2}^n$. Otherwise, at the times when $k_{i+3/2}^A$ jumps to 0.5, the pressure increases proportional to Δt . As expected, the increase in out-flux causes the pressure to decrease in the left cell (Figures 14a-14b) and the same increase in in-flux causes the pressure in the right cell to increase (Figures 15a-15b).

The results in this subsection demonstrate that standard use of the harmonic and arithmetic averages, commonly used in finite volume methods with variable coefficients, do not perform well for this degenerate parabolic problem.

5.2. Integral Average

In van der Meer et al. [2], the integral average

$$k_{j+1/2}^I = \frac{\int_{p_j}^{p_{j+1}} k(\tilde{p}) d\tilde{p}}{p_{j+1} - p_j}, \quad (5.8)$$

is proposed to improve upon the arithmetic average. The integral average is derived by expressing the coefficient $k(p) = \Phi_p$ in Eqn. (1.1) to obtain

$$p_t = \nabla \cdot (\Phi_p \nabla p).$$

Discretizing Φ_p directly with central differences at the cell face $x_{j+1/2}$ gives

$$k_{j+1/2}^I = \frac{\Phi(p_{j+1}) - \Phi(p_j)}{p_{j+1} - p_j}. \quad (5.9)$$

Using the definition of $\Phi(p) = \int_0^p k(\tilde{p}) d\tilde{p}$, Eqn. (5.9) simplifies to Eqn. (5.8).

As a side note, we show that we can express the scheme with integral averaging in terms of a well-known discretization to provide directions for further development. We substitute the integral average $k_{j+1/2}^I$ in Eqn. (5.8) into the finite volume semi-discrete discretization to obtain

$$\begin{aligned} \Delta x \frac{dp_j}{dt} &= - \frac{\int_{p_{j-1}}^{p_j} k(\tilde{p}) d\tilde{p}}{p_j - p_{j-1}} \frac{p_j - p_{j-1}}{\Delta x} + \frac{\int_{p_j}^{p_{j+1}} k(\tilde{p}) d\tilde{p}}{p_{j+1} - p_j} \frac{p_{j+1} - p_j}{\Delta x} \\ &= \frac{\int_0^{p_{j-1}} k(\tilde{p}) d\tilde{p} - 2 \int_0^{p_j} k(\tilde{p}) d\tilde{p} + \int_0^{p_{j+1}} k(\tilde{p}) d\tilde{p}}{\Delta x} \\ &= \frac{\Phi(p_{j-1}) - 2\Phi(p_j) + \Phi(p_{j+1})}{\Delta x}, \end{aligned}$$

for $2 \leq j \leq N$. Dividing both sides by Δx recovers the second order central discretization of the one-dimensional laplacian on a uniform Cartesian grid.

The numerical solution with the integral average is provided in Figures 16 and 17. The integral average does not introduce high frequency oscillations near p^* . The low frequency, grid-dependent oscillations remain, however. The amplitude of these oscillations is smaller than those with arithmetic averaging. The numerical solution is now monotonically increasing in time [2], matching the behavior of the true solution. Figure 6 shows that the SAM numerical solution sharply captures the discontinuity in the temporal plot, whereas the numerical solution with integral

averaging in Figure 16 is sloped. The diffusive shock profile with the integral average is also illustrated in the spatial results in Figure 17.

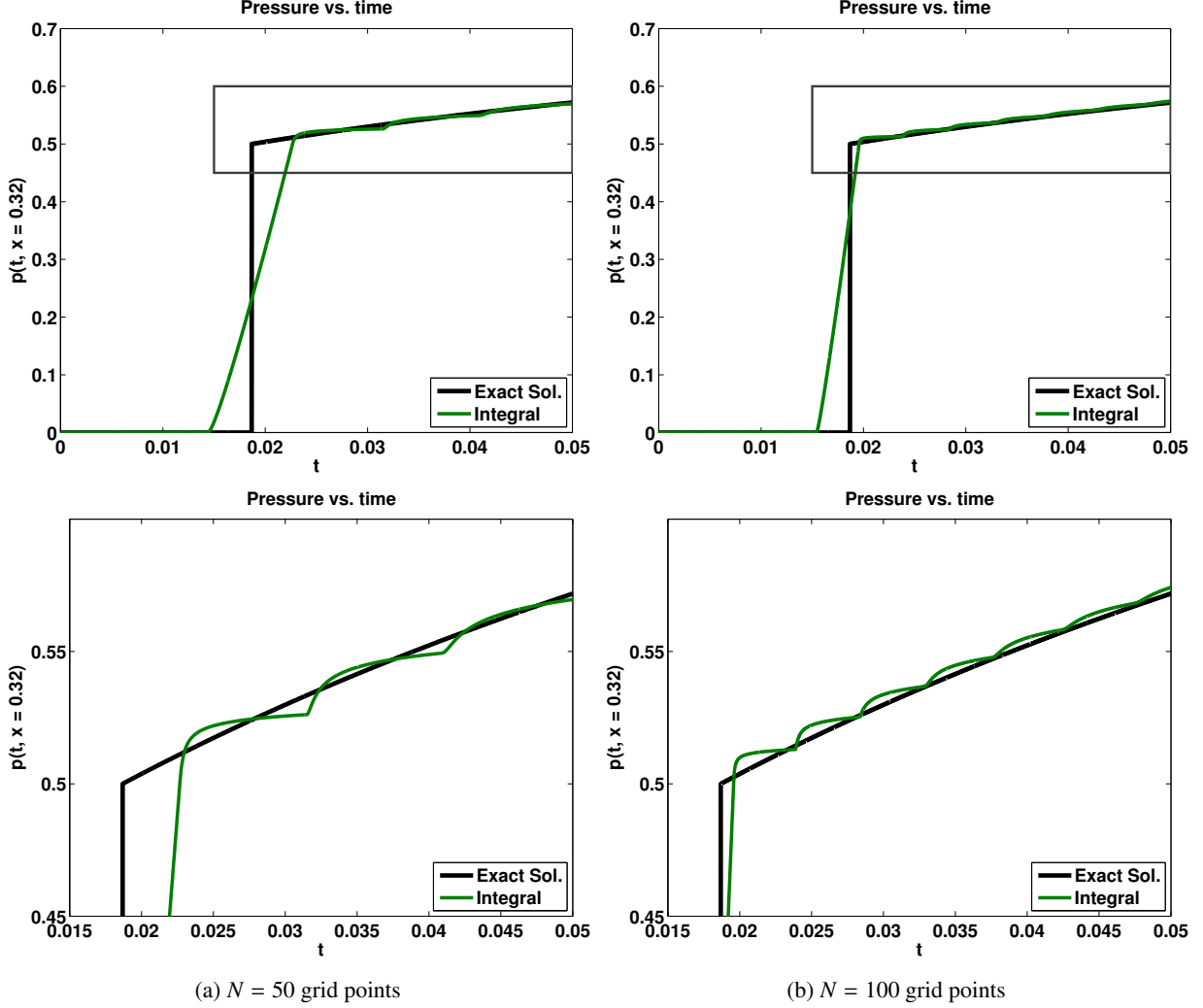


Figure 16: Temporal profiles at position $x = 0.32$ with $\Delta t = \Delta x^2/32$.

An advantage of the scheme with integral averaging is that it contains some information about the shock, as encoded in the bounds of the integral. The integral average $k_{i+1/2}^I$ in Eqn. (5.8) can be broken up at the pressure shock point p^* into two separate integrals to obtain

$$k_{i+1/2}^I = \frac{k_{\min}(p_{i+1} - p^*) + k_{\max}(p^* - p_i)}{p_{i+1} - p_i}. \quad (5.10)$$

Unlike the harmonic and arithmetic average, the integral average monotonically increases as the shock advances through the interval $[x_i, x_{i+1}]$.

The corresponding continuous flux is given by

$$F_i^{+I} = F_{i+1}^{-I} = -\frac{k_{\min}(p_{i+1} - p^*) + k_{\max}(p^* - p_i)}{\Delta x}. \quad (5.11)$$

By utilizing the pressure value at the shock, the integral flux does not compute the pressure gradient across the jump,

as done in the schemes with arithmetic and harmonic averaging. Due to the incorporation of p^* into the scheme, the high frequency oscillations near p^* present with arithmetic averaging are not present with the integral average.

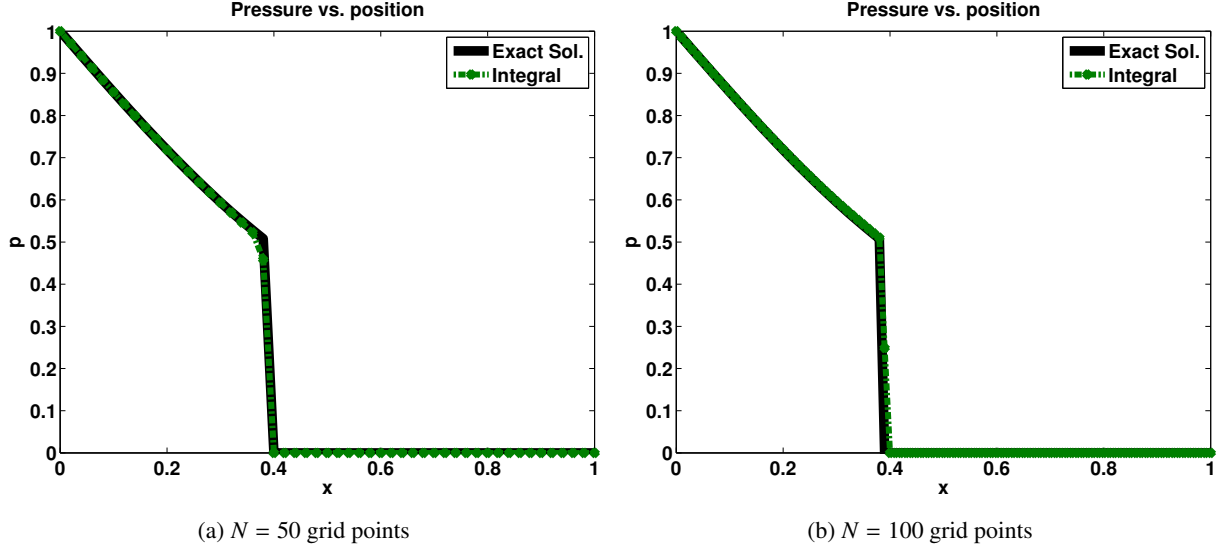


Figure 17: Spatial profiles at time $t = 0.05$ with $\Delta t = \Delta x^2/32$.

There are limitations in the integral averaging approach, as illustrated by the presence of the grid-dependent temporal oscillations in Figure 16. We see from the flux $F_{i+1/2}^I$ in Eqn. (5.11) that even though the pressure value at the shock p^* is incorporated into the scheme, the shock position $x^*(t)$ is not incorporated. In the case, where $k_{\min} = 0$, $F_i^{+I} = F_{i+1}^{-I}$ in Eqn. (5.11) appears to be similar to F_i^+ in Eqn. (2.5). The difference occurs in the denominator, where the relative shock position $\Delta x^*(t)$ detected in SAM is replaced with Δx in the integral flux. The integral flux is then assuming that the distance to the shock is fixed of size Δx .

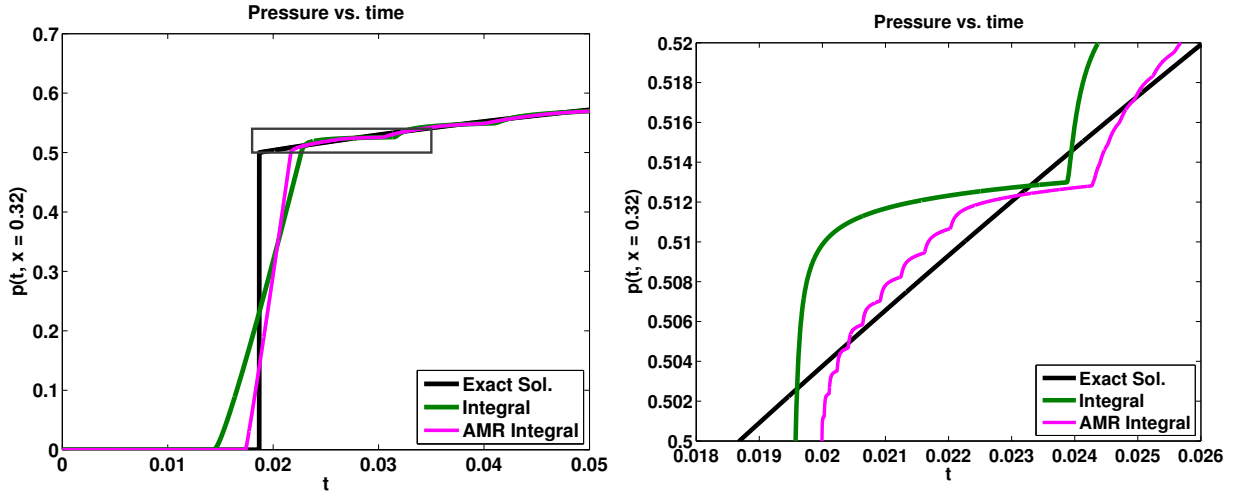


Figure 18: Temporal profiles at position $x = 0.32$ with $\Delta t = \Delta x^2/32$ and $N = 50$ coarse grid points and 10 inner grid points.

We also implement the scheme with integral averaging and Adaptive Mesh Refinement (AMR) [26]. We define a coarse mesh away from the shock and a fine mesh near the shock. The fine mesh travels with the shock as it moves.

In Figure 18, a coarse mesh size of $\Delta x = 1/50$ is utilized. Within the coarse mesh cells surrounding the shock, a fine inner mesh size of $\Delta x_{\text{inner}} = 1/10$ is defined.

Figure 18 displays that oscillations are present with a smaller period and damped amplitude. The zoomed in results in Figure 18 illustrate that there are ten oscillations in between the coarse grid cells, as expected as the front crosses the ten inner grid cells for $\Delta x_{\text{inner}} = 1/10$. The temporal oscillations are spatially dependent and so applying AMR does not remove them.

5.3. SAM in Finite Volume Average Form and its Connection to the Integral Average

Now, we will look at how we can write SAM from Section 2 as an averaged-based approach on a uniform Cartesian grid of spatial step size Δx . For $j \neq i$, we have defined $k_{j+1/2}^{SAM}$ by Eqn. (2.4) in Section 2. The Cartesian and auxiliary grids are the same in the parabolic regions away from the shock. The difference between the grids occurs in the interval $[x_i, x_{i+1}]$ containing the shock. Using Eqns. (2.5) - (2.6), we can write the out-flux F_i^+ of CV_i and the in-flux F_{i+1}^- of CV_{i+1} for SAM in finite volume average form as

$$F_i^+ = - \underbrace{\left(k_{\max} \frac{\Delta x}{\Delta x^*} \frac{p^* - p_i}{p_{i+1} - p_i} \right)}_{k_{i+1/2}^{SAM^+}} \frac{p_{i+1} - p_i}{\Delta x}, \quad (5.12)$$

and

$$F_{i+1}^- = - \underbrace{\left(k_{\min} \frac{\Delta x}{\Delta x - \Delta x^*} \frac{p_{i+1} - p^*}{p_{i+1} - p_i} \right)}_{k_{i+1/2}^{SAM^-}} \frac{p_{i+1} - p_i}{\Delta x}, \quad (5.13)$$

respectively.

The uniform Cartesian grid has less information than the auxiliary grid, since it does not contain the control volume CV_* surrounding the shock. As a result, to capture the same out-flux of CV_i in Eqn. (2.5) and in-flux of CV_{i+1} in Eqn. (2.6), we define the above two distinct fluxes at the interface $x_{i+1/2}$.

There is a relation between the averages defined by SAM and the integral average. We can express the SAM averages as the following weighted linear combinations of the integral average $k_{i+1/2}^I$ in Eqn. (5.10),

$$c_1 \frac{k_{\min}(p_{i+1} - p^*)}{p_{i+1} - p_i} + c_2 \frac{k_{\max}(p^* - p_i)}{p_{i+1} - p_i}.$$

For $c_1 = 0$ and $c_2 = \Delta x / \Delta x^*$, $k_{i+1/2}^{SAM^+}$ in Eqn. (5.12) is recovered, while for $c_1 = \Delta x / (\Delta x - \Delta x^*)$ and $c_2 = 0$, $k_{i+1/2}^{SAM^-}$ in Eqn. (5.13) is recovered.

We can also express the integral flux in terms of the SAM fluxes surrounding the shock cell. Rewriting Eqn. (5.11), we have

$$\begin{aligned} F_i^{+I} &= - \left[k_{\min} \frac{p_{i+1} - p^*}{\Delta x - \Delta x^*} \frac{\Delta x - \Delta x^*}{\Delta x} + k_{\max} \frac{p^* - p_i}{\Delta x^*} \frac{\Delta x^*}{\Delta x} \right] \\ &= F_{i+1}^-(1 - y) + F_i^+ y, \end{aligned} \quad (5.14)$$

where $y \equiv \Delta x^* / \Delta x$. The shock moves from left to right in the interval $[x_i, x_{i+1}]$, and $0 < y < 1$. Below, we use a representative example for a specific y to show that the integral flux does not converge to the analytical flux.

Without loss of generality, we let the shock be to the right of the cell face $x_{i+1/2}$ by $\epsilon \Delta x$ for some small $\epsilon > 0$. Then $y = 1/2 + \epsilon$. Using Taylor series expansion in the parabolic region to the left of the shock gives

$$F_i^+ = F^L[p(x_{i+1/2+\epsilon})] + \mathcal{O}(\Delta x), \quad (5.15)$$

where $F^L[p(x)] = -k_{\max} \nabla p(x)$. Similarly, Taylor series expansion in the parabolic region to the right of the shock gives

$$F_{i+1}^- = F^R[p(x_{i+1/2+\epsilon})] + \mathcal{O}(\Delta x), \quad (5.16)$$

where $F^R[p(x)] = -k_{\min}\nabla p(x)$. Substituting Eqns. (5.15)-(5.16) into Eqn. (5.14) gives the following

$$F_i^{+I} = F^R[p(x_{i+1/2+\epsilon})](0.5 - \epsilon) + F^L[p(x_{i+1/2+\epsilon})](0.5 + \epsilon) + O(\Delta x).$$

Taking the limit as $\epsilon \rightarrow 0$, we obtain

$$F_i^{+I} = \frac{F^R[p(x_{i+1/2})] + F^L[p(x_{i+1/2})]}{2} + O(\Delta x),$$

as the integral flux at the interface $x_{i+1/2}$. The analytical flux at $x_{i+1/2}$ is given by $F^L[p(x_{i+1/2})]$. The integral flux is then averaging the exact flux with the flux across the jump, resulting in the temporal oscillations. The integral flux does not converge to the analytical flux $F^L[p(x_{i+1/2})]$ at the interface, while the SAM flux in Eqn. (5.15) is a first-order approximation to this analytical flux.

6. Conclusions and Future Work

This paper demonstrates that the numerical challenges in discretizations of the discontinuous Generalized Porous Medium Equation (GPME) are not arising from the type of average chosen, and that the schemes cannot be compared based on averaging alone. The FTCS scheme with integral averaging performs better than the scheme with harmonic and arithmetic averaging because it has some information about the shock encoded in it, namely p^* . The shock position is not incorporated into the scheme with integral averaging, and the jump condition for integral conservation laws is not satisfied. As a result, monotonic grid size dependent temporal oscillations are still present with the integral average. In the proposed Shock-Based Averaging Method (SAM) tracking the front position, using the jump condition is the key to a numerical solution without artifacts. Once the shock position is computed, any average can be used on the auxiliary grid to result in accurate and smooth temporal profiles.

Future work includes extensions to higher dimensions and to the Porous Medium Equation (PME) subclass. Since the velocity for the GPME is given for arbitrary dimensions, it can be used as input to a level set implementation for extensions to higher dimensions, as discussed in Section 4. The level set method is a desirable approach because it is robust, and handles sharp interfaces and topological changes. The PME subclass occurs for continuous coefficients, as discussed in [1]. For these problems, as the exponent is increased, the solutions become less regular and front formation occurs. There is no known specified pressure value at the shock, as given by p^* in this problem. With the additional control volume around the shock in the auxiliary finite volume grid from Section 2, $p^*(t)$ can be solved for as an additional degree of freedom. Once the pressure shock value is detected, a similar approach as described in Section 4 can be taken, since the speed of the front is known.

Appendix A. Exact Solution Derivation for arbitrary parameters

For the test problem with the initial condition in Figure 5, the exact solution is known and is used for testing the numerical methods. The derivation given in [27] is generalized for arbitrary k_{\max} . The domain is partitioned into $\Omega_1 = (0, x^*(t))$ and $\Omega_2 = [x^*(t), \infty)$. The problem can be subdivided into two constant coefficient heat equations [27, 28]. The pressure is monotonically non-increasing and so in Ω_1 , $p_1(x, t) > p^*$ and in Ω_2 , $p_2(x, t) \leq p^*$. It can be verified that $p_1(x, t) = 1 - c_1\Phi(x/(2\sqrt{k_{\max}t}))$ and $p_2(x, t) = c_2(1 - \Phi(x/(2\sqrt{k_{\min}t}))$ for some constants c_1, c_2 to be determined. $\Phi(x) = \text{erf}(z) = \int_0^z \phi(y)dy$ is the standard Gaussian error function, where $\phi(y) = \frac{2}{\sqrt{\pi}} \exp(-y^2)$.

The unknown shock location ($x^*(t)$) needs to be computed. To do so, two additional boundary conditions are required at the shock $x = x^*(t)$, namely

1. $p_1(x^*(t), t) = p_2(x^*(t), t) = p^*$, $\forall t$ (Continuity)
2. $k_{\max}(\partial p_1(x^*(t), t)/\partial x) = k_{\min}(\partial p_2(x^*(t), t)/\partial x)$, $\forall t$ (Flux Continuity).

Since Condition (1) must hold for all t , $x^*(t) = \alpha\sqrt{t}$,

$$c_1 = \frac{1 - p^*}{\Phi(\alpha/(2\sqrt{k_{\max}}))}, \quad c_2 = \frac{p^*}{1 - \Phi(\alpha/(2\sqrt{k_{\min}}))}.$$

Condition (2) is used to derive a nonlinear solve for the remaining unknown, α . Substituting in the expressions for the derivatives and simplifying leads to

$$c_1 \sqrt{k_{\max}} \phi\left(\frac{\alpha}{2\sqrt{k_{\max}}}\right) = c_2 \sqrt{k_{\min}} \phi\left(\frac{\alpha}{2\sqrt{k_{\min}}}\right). \quad (\text{A.1})$$

Let $z_1 = \alpha/(2\sqrt{k_{\max}})$ and $z_2 = \alpha/(2\sqrt{k_{\min}})$. We substitute the expressions for c_1 and c_2 into Eqn. (A.1), multiply both sides by $\frac{\alpha}{2}$ and simplify to obtain

$$\begin{aligned} \frac{1-p^*}{\Phi(z_1)} \sqrt{k_{\max}} \phi(z_1) &= \frac{p^*}{1-\Phi(z_2)} \sqrt{k_{\min}} \phi(z_2) \iff \\ (1-p^*)(1-\Phi(z_2)) \exp(z_2^2) \frac{\alpha}{2\sqrt{k_{\min}}} &= p^* \frac{\alpha}{2\sqrt{k_{\max}}} \Phi(z_1) \exp(z_1^2) \iff \\ (1-p^*)(1-\Phi(z_2)) \exp(z_2^2) z_2 &= p^* \Phi(z_1) z_1 \exp(z_1^2). \end{aligned} \quad (\text{A.2})$$

By a Series Expansion from integration by parts,

$$1 - \Phi(z_2) = \frac{\exp(-z_2^2)}{z_2 \sqrt{\pi}} \left(1 - \frac{1}{2z_2^2} + \frac{3}{4z_2^4} - \dots \right).$$

Using the above expression, Eqn. (A.2) simplifies to

$$\frac{1-p^*}{\sqrt{\pi}} \left(1 - \frac{1}{2z_2^2} + \frac{3}{4z_2^4} - \dots \right) = p^* \Phi(z_1) z_1 \exp(z_1^2). \quad (\text{A.3})$$

In our application and most of the numerical tests, $k_{\min} = 0$. This implies that $z_2 \rightarrow \infty$. The limit as $z_2 \rightarrow \infty$ of the left hand side of Eqn. (A.3) is simply $(1-p^*)/\sqrt{\pi}$. This is an advantage of computing the series form, since we can easily take this limit as $k_{\min} \rightarrow 0$. This form is also preferred numerically when k_{\min} is small to avoid multiplication of the large $\exp(z_2^2)z_2$ terms. For the $k_{\min} = 0$ case, the unknown (α) only appears in z_1 on the right hand side of the equation, given by

$$\frac{1-p^*}{\sqrt{\pi}} = p^* \Phi(z_1) z_1 \exp(z_1^2). \quad (\text{A.4})$$

A simple one-dimensional nonlinear equation solver can be used to solve this equation for z_1 , where $\alpha = 2\sqrt{k_{\max}}z_1$.

Acknowledgements

This material is based upon work supported by the National Science Foundation Graduate Research Fellowship under Grant No. DGE - 114747.

References

References

- [1] D. Maddix, L. Sampaio, M. Gerritsen, Numerical Artifacts in the Generalized Porous Medium Equation: Why Harmonic Averaging Itself is Not to Blame, submitted, 2017 (arXiv:1709.02581).
- [2] J. van der Meer, J. Kraaijevanger, M. Möller, J. Jansen, Temporal oscillations in the simulation of foam enhanced oil recovery, ECMOR XV - 15th European Conference on the Mathematics of Oil Recovery (2016) 1–20.
- [3] K. Lipnikov, G. Manzini, D. Moulton, M. Shashkov, The Mimetic Finite Difference Method for Elliptic and Parabolic Problems with a Staggered Discretization of Diffusion Coefficient, Journal of Computational Physics 305 (2016) 111–126.
- [4] J. Vázquez, The Porous Medium Equation, The Clarendon Press, Oxford University Press, Oxford, Mathematical Theory, 2007.
- [5] K. Brattkus, D. Meiron, Numerical Simulations of Unsteady Crystal Growth, SIAM J. Appl. Math. 52 (5) (1992) 1303–1320.
- [6] J. Sethian, J. Strain, Crystal Growth and Dendritic Solidification, Journal of Computational Physics 98 (1992) 231–253.
- [7] S. Chen, B. Merriman, S. Osher, P. Smereka, A Simple Level Set Method for Solving Stefan Problems, Journal of Computational Physics 135 (1997) 8–29.

- [8] C. Ngo, W. Huang, A Study on Moving Mesh Finite Element Solution of the Porous Medium Equation, *Journal of Computational Physics* 331 (arXiv:1605.03570) (2017) 357–380.
- [9] J. Fischer, G. Günther, Finite speed of propagation and waiting times for the stochastic porous medium equation: A unifying approach, *SIAM Journal on Mathematical Analysis* 47 (1) (2015) 825–854.
- [10] S. Angenent, Analyticity of the Interface of the Porous Media Equation After the Waiting Time, *Proceedings of the American Mathematical Society* 102 (2) (1988) 329–336.
- [11] S. Antontsev, S. Shmarev, *Evolution PDEs with Nonstandard Growth Conditions: Existence, Uniqueness, Localization, Blow-up*, Atlantis Press, Amsterdam; Paris, 2015.
- [12] J. Vazquez, Numerical Simulations of Unsteady Crystal Growth, *SIAM J. Appl. Math.* 52 (5) (1992) 1303–1320.
- [13] D. Maddix, M. Gerritsen, L. Sampaio, A. Nissen, Harmonic versus Arithmetic Averaging in Reservoir Modeling, In Preparation .
- [14] A. Berger, H. Brezis, J. Rogers, A Numerical Method For Solving the Problem $u_t - \Delta f(u) = 0$, R.A.I.R.O. Analyse numérique/Numerical Analysis 13 (4) (1979) 297–312.
- [15] A. Kharab, A Numerical Solution of a Free-Boundary Problem on the Unsaturated Flow of Liquids in Porous Media, *Computers and Mathematics with Applications* 12A (12) (1986) 1193–1200.
- [16] Rizwan-uddin, An Approximate-Solution-Based Numerical Scheme for Stefan Problem with Time-Dependent Boundary Conditions, *Numerical Heat Transfer, Part B* 33 (3) (1998) 269–285.
- [17] J. Caldwell, S. Savović, Y. Kwan, Nodal Integral and Finite Difference Solution of One-Dimensional Stefan Problem, *Journal of Heat Transfer* 125 (2003) 523–527.
- [18] M. Rose, An implicit enthalpy scheme for one-phase Stefan problems, *Journal of Scientific Computing* 5 (2) (1990) 1691–85.
- [19] M. Rose, An enthalpy scheme for Stefan problems in several dimensions, *Applied Numerical Mathematics* 12 (1993) 229–238.
- [20] J. Sethian, S. Osher, Fronts Propagating with Curvature-Dependent Speed: Algorithms Based on Hamilton-Jacobi Formulations, *Journal of Computational Physics* 79 (1988) 12–49.
- [21] Y. Zhao, C. Zhao, Z. Xu, H. Xu, Modeling Metal Foam Enhanced Phase Change Heat Transfer in Thermal Energy Storage by Using Phase Field Method, *International Journal of Heat and Mass Transfer* 99 (2016) 170–181.
- [22] S. Jaisankar, S. R. Rao, A central Rankine-Hugoniot solver for hyperbolic conservation laws, *Journal of Computational Physics* 228 (2009) 770–798.
- [23] S. Gottlieb, C. Shu, Total Variation Diminishing Runge-Kutta Schemes, *Mathematics of Computation* 67 (221) (1998) 73–85.
- [24] M. Namdar Zanganeh, J. Kraaijevanger, H. Burrman, J. Jansen, W. Rossen, Challenges in adjoint-based optimization of a foam EOR process, *Computational Geosciences* 18 (3-4) (2014) 563–577.
- [25] W. Rossen, S. Zeilinger, J.-X. Shi, M. Lim, Simplified Mechanistic Simulation of Foam Processes in Porous Media, *SPE J* 4 (3) (1999) SPE-57678-PA.
- [26] M. Berger, J. Olinger, Adaptive Mesh Refinement for Hyperbolic Partial Differential Equations, *Journal of Computational Physics* 53 (3) (1984) 484–512.
- [27] J. Kraaijevanger, On the analytical solution of a quasi-linear 1-dimensional heat equation, 2011.
- [28] J. Crank, *Free and moving boundary problems*, Clarendon Press, Oxford, 1984.